Morphologies of Large-Pore Periodic Mesoporous Organosilicas

Xiao Ying Bao and X. S. Zhao*

Department of Chemical and Biomolecular Engineering, National University of Singapore, 10 Kent Ridge Crescent, Singapore 119620

Received: January 25, 2005; In Final Form: March 31, 2005

In this article, we report a systematic investigation on the morphologies of SBA-15 type large-pore periodic mesoporous organosilicas templated by the block copolymer P123. By tuning synthetic parameters such as stirring, acidity, reaction ratio, reaction duration, and autoclaving, a wide spectrum of unique primary particle morphologies, such as the spindle-, pearl-, diamond-, rod-, and platelike particles, and nanoparticles has been prepared. These primary particles were found to self-assemble in solution to form various large hierarchical macrostructures, such as mesostructured necklaces and cobweb-supported necklaces. The assembling process was elucidated with the information observed at different stages of reaction. Stirring, reaction duration, and autoclaving were identified to be the key factors affecting the efficiency and degree of the self-assembly process. A nucleation-accretion mechanism for the formation of various PMO primary particles was proposed by examining the relation between the external morphologies and the underlying mesostructure.

1. Introduction

Recently, there has been a great deal of research interest in surfactant-mediated synthesis[1] of periodic mesoporous organosilicas (PMOs) by hydrolysis and condensation of bridged silsesquinoxanes $(RO)_3-Si-R'Si-(RO)_3$.[2−15] With organic functionality R' uniformly embedded in silicate matrix, PMOs exhibit combined advantages of periodic mesoporous materials[1] and hybrid inorganic−organic materials,[11−13] thus offering many unique physicochemical properties[16,17] and gaining considerable attention in developing new generation of electronic, catalytic, adsorptive, and nanostructured materials.[17−23]

So far, the MCM-41 type PMOs with a 2D hexagonal structure (*P6mm*) have been widely studied because of the relatively well-understood synthesis chemistry.[2−4] With the emergence of large-pore SBA-15 type periodic mesoporous silicas (PMSs) synthesized in the presence of nonionic poly-(ethylene oxide) (PEO) surfactants or triblock copolymers as the templates,[24] the SBA-15 type PMOs have attracted lots of recent attention because of their larger pore sizes ranging from 6 to 30 nm, better chemical and physical stabilities, and cheaper surfactant templates used. However, earlier attempts[5−7] to synthesize large-pore PMOs ended up with limited success in obtaining high-quality SBA-15 PMOs, in part because the authors essentially followed the synthetic recipe of SBA-15 PMSs, which employs relative strong acidic conditions.[24] Subsequently, special synthetic techniques such as true-liquid-crystal templating,[25] salt-assisted synthesis,[26] and solvent-assisted synthesis[27] have been demonstrated. In a very recent study,[28] we have reported a low-acid-concentration synthetic strategy without involving any additives, which affords high-quality SBA-15 PMOs. In addition to the role that acid plays in the formation of SBA-15 PMO mesostructures, the organic spacers R' have been identified to be a key parameter to be considered when designing and synthesizing SBA-15 PMSs.[28]

Morphological control over mesoporous materials is important for applications such as biomolecule immobilizations,[29,30]

* To whom correspondence should be addressed. E-mail: chezxs@nus.edu.sg.

cosmetics,[31] chromatography,[32] and optical applications.[33] PMSs with various morphologies such as rods,[34−36] fibers,[37−39] spheres,[40−43] gyroids,[44−46] hollow tubes,[47] vesicles,[48] and cubes[49] have been reported. Similarly, cationic-surfactant-templated PMOs with morphologies akin to those of PMSs, such as gyroids, discoids, ropes, rods, spheres, and truncated rhombic dodecahedras, have also been available.[50−53] However, till now, a systematic study on the morphologies of large-pore PMOs has not been reported.

In this work, the morphological evolution of SBA-15 PMOs with respect to the synthesis conditions was investigated. The effects of synthetic parameters, such as stirring, acidity, reaction ratio, reaction duration, and autoclaving, on particle morphologies were examined. SBA-15 PMSs were also involved for comparison purposes. Various ropelike hierarchical macrostructures self-assembled from primary particles in spindle-, pearl-, diamond-, or rodlike shapes were obtained. The assembling process was elucidated by directly observing the primary particles at different stages of reaction. Stirring, reaction duration, and autoclaving were identified to be the key factors affecting the efficiency and degree of such self-assembly. On the basis of existing theories,[40−46,54] the formation mechanism of the various PMO primary particles was suggested by examining the relationship between particle morphologies and the underlying mesostructures with the techniques of field-emission scanning electron microscopy (FE-SEM) and transmission electron microscopy (TEM).

2. Experimental Section

2.1. Chemicals and Synthesis. 1,2-Bis(trimethoxysilyl)ethane (BTMSE, 96%, Aldrich), tetraethyl orthosilicate (TEOS, 98%, Fisher), triblock copolymer $EO_{20}PO_{70}EO_{20}$ (Pluronic P123, Aldrich), fuming hydrochloric acid (HCl, 37%, Merck), and absolute ethanol (99.98%, Merck) were used as received.

The SBA-15 PMOs were synthesized as described previously.[28] A typical synthesis of SBA-15 PMO is briefed here. P123, 0.5 g, was combined with 7 mL of deionized water under stirring at 40 °C. BTMSE, 0.656 mL, was added to a mixture containing 7 mL of deionized water and 1.2 mL of 1.0 M HCl

TABLE 1: Molar Compositions for Synthesizing MSE*y* and OS*y* Materials

sample	Si	P123	HCl	H_2O	HCl/H_2O	Si/P123
MSE1, OS1	1.00	0.0173	0.048	168	2.86×10^{-4}	58
MSE2, OS2	1.00	0.0173	0.119	168	7.08×10^{-4}	58
MSE3, OS3	1.00	0.0173	0.243	168	1.45×10^{-3}	58
MSE4, OS4	1.00	0.0173	0.490	168	2.92×10^{-3}	58
MSE5, OS5	1.00	0.0173	1.064	168	6.33×10^{-3}	58
MSE6, OS6	1.00	0.0173	3.773	168	2.25×10^{-2}	58
MSE40	1.00	0.0208	0.490	168	2.92×10^{-3}	48
MSE41	1.00	0.0139	0.490	168	2.92×10^{-3}	72
MSE42	1.00	0.0103	0.490	168	2.92×10^{-3}	97

at 40 °C. The P123−H_2O solution was then slowly added to the BTMSE−H_2O−HCl mixture to obtain another mixture with a molar composition of Si:P123:HCl:H_2O = 1.00:0.0173:0.243: 168. After stirring for 24 h at 40 °C, the slurry was transferred into a polypropylene bottle and heated at 100 °C for 120 h. The white solids were recovered by filtration, washed with deionized water and ethanol, and dried under ambient conditions.

The concentration of HCl was varied to obtain different HCl/H_2O molar ratios ranging from 2.86×10^{-4} to 2.25×10^{-2}. Precipitate was not observed within 1 day from synthesis systems having HCl/H_2O molar ratios lower than 2.86×10^{-4}. The SBA-15 PMO samples thus prepared are denoted as MSE*y*, where MSE denotes the organosilica precursor BTMSE and *y*, ranging from 1 to 6, indicates the molar ratios of HCl/H_2O in the synthesis gels. By maintaining a constant HCl/H_2O molar ratio at 2.92×10^{-3}, another set of SBA-15 PMO samples was synthesized by varying the molar ratios of Si/P123. The samples thus prepared are designated as MSE40, MSE4, MSE41, and MSE42, representing the samples synthesized with Si/P123 = 48, 58, 72, and 97, respectively.

A morphokinetic study was carried out using a representative material MSE3. The synthetic mixture during stirring was taken out from the synthesis system after reaction started for 5, 7.6, 9.6, and 24 h, followed by filtering, washing, and drying. The samples are designated as MSE3-*t*h, where *t* indicates the stirring times, namely, 5, 7.6, 9.6, and 24 h.

To find out the effect of stirring on morphology, a sample was prepared with the identical synthesis parameters to MSE3 but without stirring. It is designated as MSE3static.

For comparison purposes, SBA-15 PMSs were also prepared using the same synthetic procedures with HCl/H_2O ratios ranging from 2.86×10^{-4} to 2.25×10^{-2} at a fixed Si/P123 molar ratio of 58. Here, two moles of TEOS were considered to be equivalent to one mole of BTMSE. The samples are designated as OS*y* with the sample meaning of *y*. The synthesis molar compositions for synthesizing the MSE*y* and OS*y* materials involved in this study are listed in Table 1. Template removal from the samples was carried out by ethanol extraction at 70 °C for 6 h under stirring.

2.2. Characterization. Small-angle X-ray scattering (SAXS) measurements were performed on a Bruker NanoStar at 40 kV and 35 mA with Cu Kα radiation of wavelength $\lambda = 1.54184$ Å. The distance between sample and detector was 1.1 m. The scattered intensities, plotted against the scattering angel 2θ, were integrated azimuthally from the scattering patterns made up of several concentric circles. Field-emission scanning electron microscopy (FE-SEM) images were obtained with a JEOL JSM-6700F microscope at an accelerating voltage of 5.0 kV. Transmission electron microscopy (TEM) images were collected on a JEOL 2010 electron microscope operated at an acceleration voltage of 200 kV. To prepare samples for TEM, a small amount of the material was first suspended in absolute alcohol by sonication in an ultrasonic water bath for 10 min. A drop of
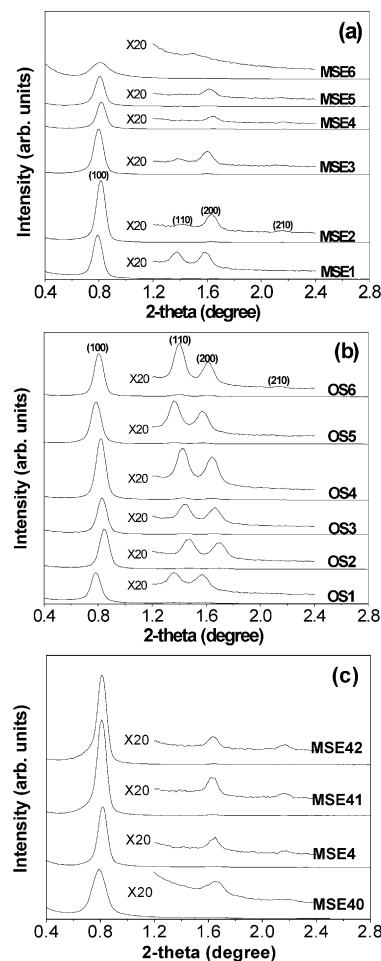

Figure 1. SAXS patterns of (a) SBA-15 PMOs synthesized at various HCl/H_2O molar ratios; (b) SBA-15 PMOs synthesized at various HCl/H_2O molar ratios; (c) SBA-15 PMOs synthesized at various Si/P123 molar ratios.

this suspension was then placed onto a carbon-coated 200-mesh copper grid, followed by drying at room temperature. To get a better TEM image of the mesostructures, ultrathin sections (∼50 nm) of samples MSE2, MSE40, and MSE42 embedded in an epoxy resin were prepared by ultramicrotomy before being deposited on a carbon-coated copper grid.

3. Results

3.1. Small-Angle X-ray Scattering. The crystallographic structure (space group: *P6mm*) of all the MSE*y* and OS*y* materials synthesized in this work was confirmed by the SAXS patterns shown in Figure 1. Apart from MSE6, which displays a broad (100) peak, all materials exhibit a sharp (100) peak and several higher order peaks, indicating a relatively good mesostructure ordering and the presence of large ordered domains. On the other hand, the broad (100) peak of MSE6 suggests a poor mesostructure ordering and small ordered domains.

A careful examination of the SAXS patterns reveals that for the MSE*y* materials synthesized with varying HCl/H_2O ratios, broadening of the (100) peak as well as a decrease in the (100) peak intensity, indicating a decreased structural ordering, can be seen on the samples synthesized with HCl/H_2O molar ratios above 2.92×10^{-3}. However, such a trend is not seen on the OS*y* materials. For the samples synthesized with various Si/P123 molar ratios, the highest (100) intensity is seen on the sample synthesized with an intermediate Si/P123 ratio, that is,
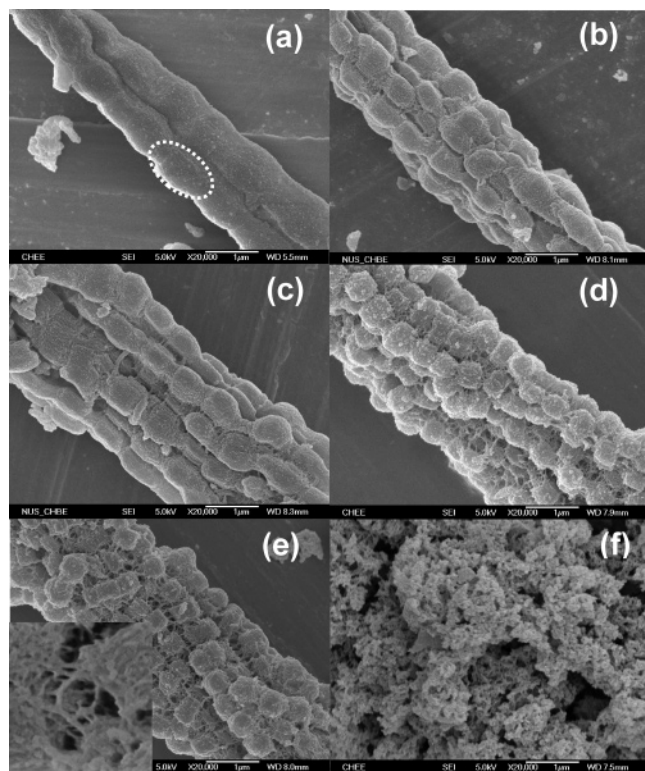
Morphologies of Periodic Mesoporous Organosilicas

J. Phys. Chem. B, Vol. 109, No. 21, 2005 **10729**

Figure 2. FE-SEM micrographs of the SBA-15 PMOs synthesized at various HCl/H$_2$O ratios: (a) MSE1, the dashed ellipse indicates a spindlelike particle resolved from a wire of the rope; (b) MSE2; (c) MSE3; (d) MSE4; (e) MSE5, insert of e shows a magnified image of the cobweblike network; and (f) MSE6.

Si/P123 = 72. A higher or a lower Si/P123 ratio led to a decreased (100) intensity. The (100) peak width of the PMOs synthesized with Si/P123 = 58−92 are comparable while a sudden broadening of the (100) peak is seen for the sample synthesized with Si/P123 = 48.

3.2. Effect of Acidity on Particle Morphology. Figure 2 shows the FE-SEM images of the PMOs prepared with various HCl/H$_2$O molar ratios. Ropelike macrostructures with lengths of ∼100 μm and diameters less than ∼5 μm are predominant for materials MSE1−MSE5. However, substantial differences among the ropelike macrostructures are evident. Materials MSE1−MSE3 feature a ropelike morphology composed of bundles of parallel running necklacelike wires. Spindlelike ellipsoids can be seen from the necklacelike wires from samples MSE1−MSE3 as highlighted in Figure 2a. The diameter of the knots of the necklaces, which is equivalent to the length of the minor axis of the spindlelike ellipsoids, was decreased from ∼0.7 μm for sample MSE1 to ∼0.5 μm for sample MSE3. On the other hand, the knot-to-neck diameter ratio of the necklace-like wires was increased from ∼1.2 for MSE1 to ∼2 for MSE3. The increased knot-to-neck ratio indicates a reduced degree of end-to-end interconnection between the spindlelike primary particles. Material MSE1 synthesized at the lowest acid concentration, for example, exhibits the largest degree of such interconnection. This is in accordance with the concept of sticky end proposed by Ozin et al.,[44] because the mesopores are running along the major axis of the spindles (see below about discussion on TEM data). According to this concept, the less acidic the synthetic gel is, the slower the condensation−polymerization rate of organosilicate species is, and thus the stickier the surfactant−organosilicate ends of the spindlelike particles is. As a result, sample MSE1 has the best intercon-nection of the primary particles.
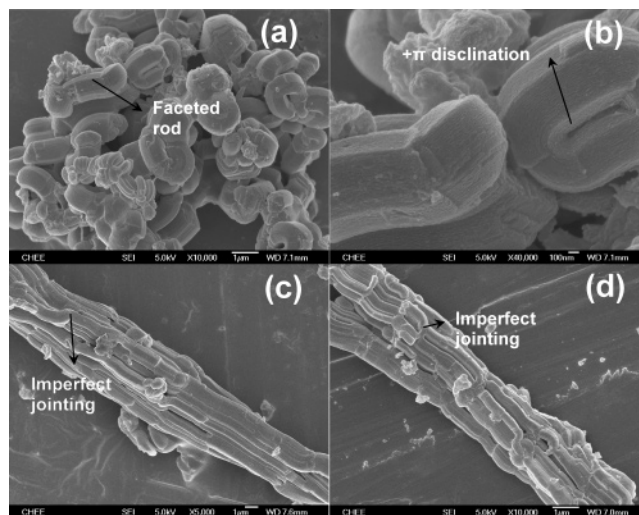

Figure 3. FE-SEM micrographs of representative SBA-15 PMSs synthesized at various HCl/H$_2$O ratios: (a) OS2, (b) OS2 of a larger magnification, (c) OS4, and (d) OS6.

Materials MSE4 and MSE5 feature near-spherical pearl-like or short cylindrical primary particles with mean diameters of ∼0.4 μm, which is smaller than the primary particles of MSE1, MSE2, and MSE3. More short cylindrical particles are seen on sample MSE5 than on sample MSE4 and the primary particle size of MSE5 is slightly smaller than that of MSE4. Loose end-to-end connection among these primary particles into many individual wires is discernible. When viewed at a higher magnification (Figure 2e, insert), it is seen that the surfaces of these pearl-like particles are much more corrugated than those observed on samples MSE1−MSE3. More interestingly, it can be seen that these discrete particles are supported by a cobweblike network, which is formed by interweaving of numerous nanofibers with diameters of about tens of nanometers not only between neighboring particles of the same wire but also between particles situating at adjacent wires. Such cor-rugations and nanofibers are more prominent for samples MSE5 than MSE4, although they are also present, but in a trivial amount, on the ropes of MSE2 and MSE3. The nature of the fibers, being hollow or solid, will be discussed in a later section. Different from other materials, a highly irregular morphology with randomly aggregated, nanosized platelets, rods, and particulates is seen on sample MSE6.

Compared with the morphologies of SBA-15 PMOs, the particle morphologies of SBA-15 PMSs are less sensitive to the variation of HCl/H$_2$O ratios used during synthesis. As can be seen from Figure 3, curved faceted rods based on elongated hexagonal prisms are the major products for samples OS1 and OS2 synthesized at relatively low-acid concentrations. The surfaces of the rods are relatively smooth; however, a close examination (Figure 3b) of the rods reveals parallel stripes running along the main axis, indicating a good alignment of the mesopore channels along the long axis of the hexagonal prism.[55] The faceted rods are highly curved, which is due to the disclinations rotated along the transverse axes in the *ab*-plane of the hexagonal prism.[45] Figure 3b, for example, features a +π disclination about a transverse axis. The average thickness of the rods is ∼0.8 μm, a size that is larger than any of the SBA-15 PMOs investigated.

The morphologies of OS3−OS6 are characterized by ropelike macrostructures assembled from many parallel running faceted wires with a constant hexagonal cross section. The faceted wires are straight and their surfaces are smooth. Upon careful
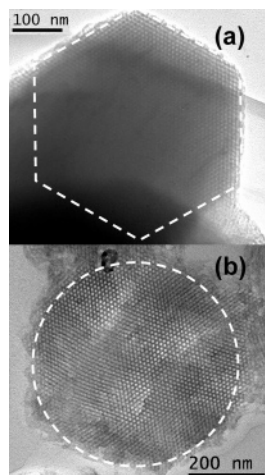
Figure 4. TEM micrographs of (a) MSE2 and (b) OS2 taken with line of vision parallel to the pore axis. The dashed hexagon and circle highlights the shape of their basal planes. Ultrathin sections (~50 nm) of sample MSE2 embedded in an epoxy resin were prepared by ultramicrotomy before being deposited on a carbon-coated copper grid.

observations, the wires were found to be connected by many rodlike straight segments. Nodes between these rodlike segments, although not obvious, are identifiable by the imperfections in the jointings (see Figure 3c, d). It was noticed that the segments running down the long axis of the ropes of OS4 can be as long as tens of micrometers, while those in OS6 are relatively shorter.

From the above discussion and comparison, the following conclusions can be drawn: (1) The cross sections of the wirelike building blocks in SBA-15 PMOs are often circular, albeit with some irregularities, while the wirelike building units in the SBA-15 PMSs are usually faceted with well-defined hexagonal cross sections. This can be further confirmed by the TEM data shown in Figure 4, which reveal the shapes of the basal planes of MSE and OS materials. (2) The cross-sectional areas of SBA-15 PMOs are varying periodically along the axis of the wires, making the wires appear necklace-shaped, while the cross sections of SBA-15 PMSs are highly uniform hexagons along the longitudinal axis of the wires. In addition, the knot-to-neck ratios of the necklace-shaped wires increase constantly with increasing acid content in the system until the "pearls" in the necklace are only loosely linked and entrapped in a cobweblike network.

3.3. Effect of Si/P123 Ratio on Particle Morphology. By increasing the Si/P123 ratio from 58 to 72 while keeping other parameters the same as MSE4, material MSE41 was obtained, which exhibits ropelike morphology made up of diamondlike particles without the presence of the cobweblike network, as can be seen from Figure 5b. Unlike the morphology of the primary particles of sample MSE4, the morphology of the primary particles of MSE41 is akin to elongated hexagonal dipyramids. The surfaces of the primary particles of MSE41 are smoother than that of sample MSE4. In addition, discrete primary particles were found on MSE41 because of the loose end-to-end connection and the absence of the cobweblike network (see Figure 5c).

When the Si/P123 ratio was further increased to 97 to obtain sample MSE42, neither the ropelike macrostructures nor the nanofibers are seen. Instead, hexagonal platelets with smooth surfaces with a mean size of ~1 μm and a thickness of ~0.4 μm are present in majority (see the inserts in Figure 5d). Many of these hexagonal platelets are broken, which could be due to the shearing force brought about by stirring. Many of these
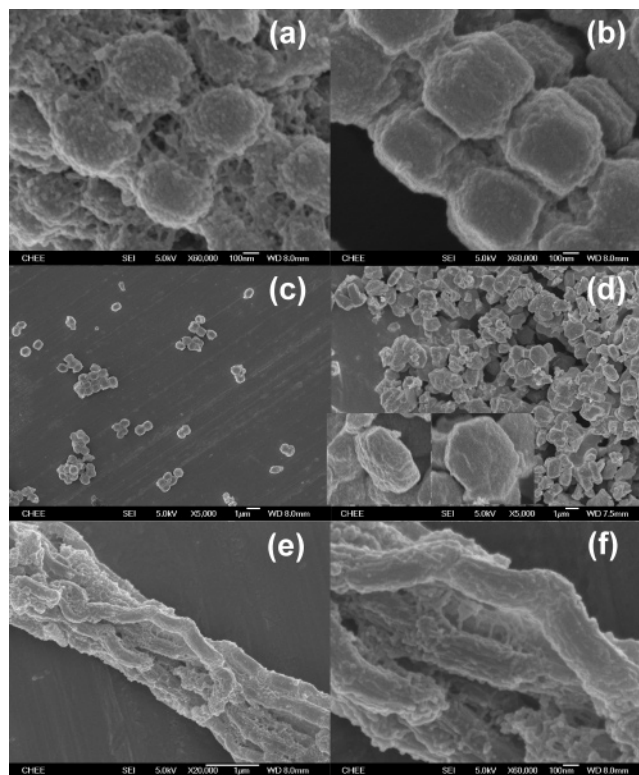

Figure 5. TEM micrographs of SBA-15 PMOs synthesized at various Si/P123 molar ratios: (a) MSE4; (b) MSE41; (c) discrete particles of sample MSE41; (d) MSE42, inserts of d show magnified images of the platelike particles; (e) MSE40; and (f) MSE40 of a larger magnification.

hexagonal platelets were melted together to form large, irregularly shaped chunks.

A decrease in Si/P123 molar ratio from 58 to 48 yielded sample MSE40 with a unique morphology. The ropelike macrostructure of MSE40 is composed of bundles of wires made from rodlike particles with a circular cross section of ~1 μm in length and ~0.2 μm in diameter (see Figure 5e). Imperfections in jointing between the rodlike particles can be identified and they often form angles less than 180° at the nodes. Similar to that of MSE4, the surface of MSE40 is corrugated. Nanofibers linking adjacent wires are also present in MSE40 (Figure 5f).

4. Discussion

4.1. Formation of Spindle- and Pearl-like Particles. As can be seen from the TEM image of Figure 4a, the six facets of the hexagonal prisms seen of SBA-15 PMSs can be indexed as the {100} surfaces, which are the most densely packed planes in a 2D hexagonal structure. These planes grow slower than other planes and dominate the final crystal morphology,[49,56] which is thermodynamically favored because they are the most stable planes. For SBA-15 PMOs as evidenced from the TEM image of MSE2, no presence of polycrystal is evident upon a TEM analysis of the cross sections of the necklacelike wires (Figure 4b); therefore, these circular cross sections reveal a fast and an isotropic growth of the organosilicate liquid-crystal embryos in all directions. The fast growth of the organosilicate liquid crystal can be justified because organosilica precursor BTMSE hydrolyzes and condenses faster than silica precursor TEOS.[28]

Viewing the spindlelike particles of MSE2 with the longitudinal axis or *c*-axis perpendicular to the direction of observation (Figure 6a), it is seen that the *c*-axis of the particle, along which the mesopore channels are running, is not parallel with
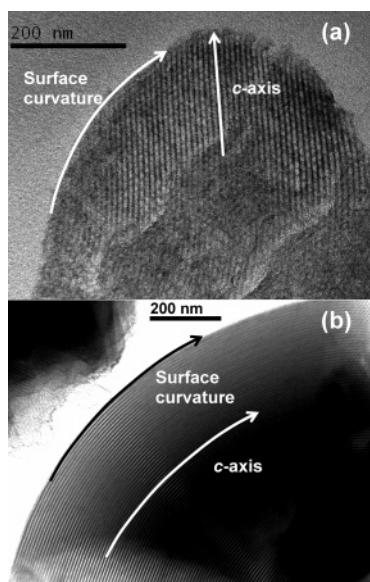
Figure 6. TEM micrographs of (a) MSE2 and (b) OS2 taken with line of vision perpendicular to the pore axis. Ultrathin sections (∼50 nm) of sample MSE2 embedded in an epoxy resin were prepared by ultramicrotomy before being deposited on a carbon-coated copper grid.

the surface curvature. The mesopore channels are longest at the major axis of the ellipsoid and their lengths decrease outward continuously from the major axis. In other words, the surface curvature results from the decrease in the length of the mesopore channels. In contrast, the surface curvature of sample OS2 seems to arise from a much different nature; its mesoporous channels run along the *c*-axis and are parallel to the surface curvature of the particle (see Figure 6b).

The spindlelike or prolate ellipsoidal morphology reported here has never been observed previously. A morphological analogue is the MCM-41 type oblate ellipsoids synthesized by co-condensation of TEOS and organosilane.[57] However, the formation mechanisms of these two types of ellipsoids are different. Preferential ordering of the mesopore channels normal to the local tangent in the near-surface regions is seen for the oblate ellipsoids,[57,58] while the mesopore channels in our spindlelike particles are parallel to the major axis of the prolate ellipsoids.

It has been proposed that the formation mechanism of mesoporous silica particles involves cooperative organization of silicates and globular micelles to form short rodlike silicate-wrapped surfactant micelles, followed by nucleation of the silicate-micelle species yielding silicatropic liquid-crystal nuclei or seeds.[59,60] Growth of the nuclei mainly occurs after a significant extent of ordering has been achieved for the nuclei.[44,46,60,61] For example, Regev observed the presence of clusters of ordered, elongated silicate-micelles at the very early stage of reaction by using cryo-TEM technique. Droplet-shaped objects with sizes of 50−70 nm and ordered, mesostructured interiors have been visualized by using AFM and TEM techniques.[46] The growth of the silicate liquid-crystal nuclei proceeds via side-by-side anchoring of the silicate-micelles onto the seeds and continuous elongation of the aggregated silicate-micelles along the long axis.[46,62] The preferred way of anchoring, however, is dependent on the defect and director filed pattern, surface mesostructure, and charges of the nuclei, which are determined by the solution environment experienced by the silicate liquid-crystal nuclei.[46]

On the basis of the above observations and discussion, the relationship between the growth mechanism of an SBA-15 PMO

such as MSE2 and its spindlelike morphology is suggested as schematically shown in Figure 7. The formation of the spindle-like particles can be divided into a few steps: (1) soon after the mixing of the reactants, a large amount of rodlike organo-silicate-micelles were formed as a result of the co-assembly between the hydrolyzed organosilica species and the surfactant micelles (Figure 7a); (2) the aggregation of several organosili-cate-micelles led to the formation of organosilicate liquid-crystal nuclei,which grew as a result of continuous accretion of the organosilicate-micelles onto the nuclei along the longitudinal axis and the transverse axes (Figure 7b). During this process, the degree of condensation of the organosilica framework was increasing continuously (indicated by increase in color dark-ness); (3) after a period of time, the growth of the crystals slowed because of polymerization of the organosilicates, resulting in diminishment of the number of hydroxyl groups, which are essential for side-by-side or end-to-end anchoring of the organosilicate-micelles along the transverse axes or the longi-tudinal axis. Such passivation also occurred for the organosili-cate-micelles that have not yet attached on the crystals (Figure 7c). Therefore, the more recently anchored organosilicate-micelles along the transverse axes were not able to grow into similar lengths as those which were anchored earlier. In other words, the organosilicate-micelle rod situated at or near the major axis of the particle would have grown into the longest mesopore channel, and the lengths of the mesopore channels decreased continuously outwardly from the major axis (Figure 7d).

It is believed that the passivation was more severe for the hydroxyl groups at the surfaces of the crystals than those at the ends, as the hydroxyl groups at the ends are relatively shielded from the acid by the surfactant micelles, thus forming the sticky ends.[44] As a result, the growth of the crystal along the longitudinal axis was able to proceed for a longer time than the growth along the transverse axis (Figure 7c, d), and this aided the formation of spindlelike particles with long major axes, instead of near-spherical particles.

Although samples MSE1−MSE5 display different particle morphologies (spindlelike and pearl-like morphologies), it is believed that they were formed following a similar mechanism as that of MSE2. The reason particles with a shorter major axis for samples MSE4 and MSE5 than for MSE1−MSE3 is probably due to the relative high-acid concentrations used for synthesizing MSE4 and MSE5. The higher acid concentration resulted in a stronger passivation effect on hydroxyl groups, leading to a less pronounced sticky end effect.[44] In other words, the pearl-like and short cylindrical shapes of materials MSE4 and MSE5 could be considered as the intermediate shape shown in Figure 7c during the formation of the particles in MSE2. The stronger acidity used for synthesizing MSE4 and MSE5 terminated particle growth at this stage.

The decrease in particle size from sample MSE1 to sample MSE6 is again due to the catalytic function of acid to the hydrolysis and condensation of the organosilica precursors.[28] A larger amount of organosilicate liquid-crystal seeds were formed under high-acid concentrations and the simultaneous growth of these seeds quickly depleted the organosilicates in the solution. An extremity of this scenario is MSE6 with numerous small particles, each containing only several poorly ordered mesopore channels as can be seen from the TEM image in Figure 8. The TEM image of MSE6 is also in agreement with its SAXS pattern shown in Figure 1, which suggests a poor mesostructure ordering and small ordered domains of this material.
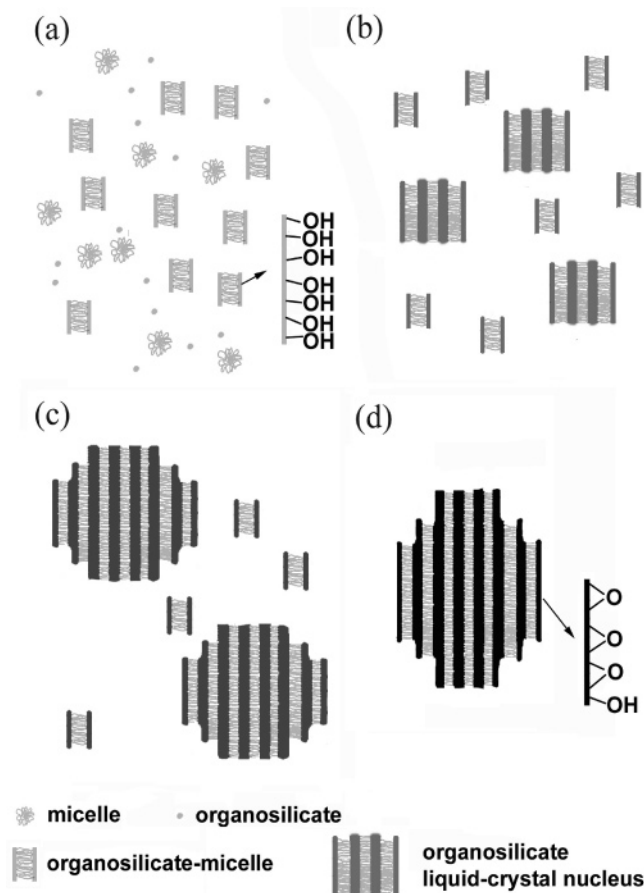
Figure 7. Schematic illustration of the nucleation-accretion process of the organosilica particles. A darker color of the PMO framework indicates a higher degree of organosilicate condensation and a lower amount of free silanols.
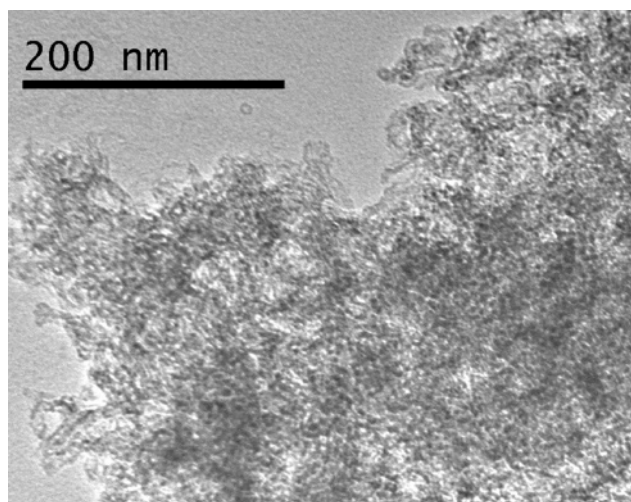

Figure 8. A TEM micrograph of sample MSE6.

4.2. Formation of SBA-15 PMS Particles. The growth of SBA-15 PMSs, on the other hand, proceeds in a slower rate than SBA-15 PMOs because of the slower condensation rate of TEOS than bridged silsesquinoxanes. The slower condensation rate of TEOS produced much lesser silicate-micelle liquid-crystal seeds initially, and this resulted in larger PMS particles than PMO particles. The formation of PMS particles with constant cross sections was favored so as to maximize the contact of the silicate-micelles. The preferred growth of the particles along the longitudinal axis, which led to the formation of long hexagonal rods, is attributed to the sticky end effect.[44]
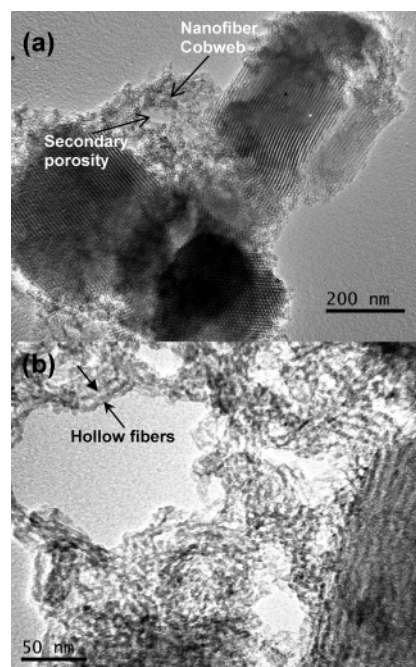

Figure 9. TEM micrographs of (a) MSE5 and (b) a magnified image of the nanofibers and the cobweblike network.

Recently, ropelike SBA-15 PMSs consisting of bundles of wires made up of interconnecting hexagonal prisms of $1-2$ μm have been reported by two research groups.[54,55] The end-to-end assembling of the rodlike particles to wires and then to ropelike macrostructure has been attributed to the shearing flow brought about by the continuous stirring, without which only dispersed hexagonal prisms of similar sizes were obtained.[55] SBA-15 PMSs with dispersed or aggregated rodlike or fiberlike morphology have also been reported by using various silica precursors with or without additives.[35−37] Although similar ropelike macrostructures were also exhibited by the SBA-15 PMSs synthesized in this work such as OS4 and OS6, the wires running down the long axis of the ropes of OS4 and OS6 are made up of much longer hexagonal rods compared with the rods of only $1-2$ μm observed previously,[54,55] that is, the low-acid synthetic conditions employed in the present work favors the formation of longer hexagonal prisms.

In the previous works,[54,55] typical HCl/H$_2$O molar ratios that yielded mesoporous rods of $1-2$ μm in length were 3.61×10^{-2} and 2.91×10^{-2}, respectively. These values are much larger than, for example, that used for synthesizing sample OS4 (HCl/H$_2$O $= 2.92 \times 10^{-3}$). Therefore, the higher acid concentrations used in the previous works[54,55] produced more seeds during the initial stage of the reaction, thus resulting in the formation of shorter hexagonal prisms. Also, higher acid concentration passivated the basal planes or the silicate-surfactant sticky ends of the growing rods earlier than those synthesized at lower acid concentrations, thus permitting only the formation of short rods.

The morphologies of material OS2, mainly consisting of highly curved faceted mesoporous rods, are largely different from those of OS4 and OS6. The increase in synthesis pH and the subsequent morphological transition from faceted rodlike morphologies to various macrostructures with high curvatures and then to spheres for MCM-41 materials synthesized in quiescent acidic environment was studied by Ozin et al.[44−46] The obtaining of highly curved SBA-15 materials including gyroids, discoids, spheres, and doughnutlike morphologies was also achieved by the addition of organic cosolvents and inorganic
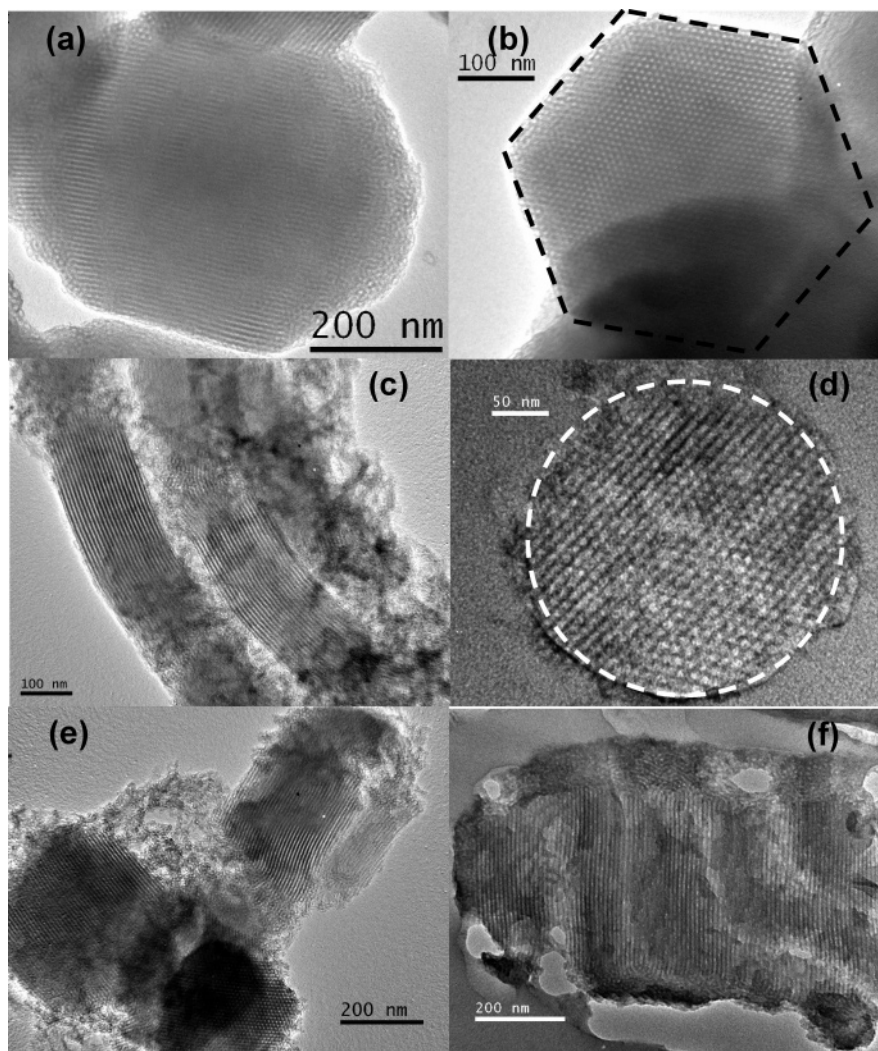
Morphologies of Periodic Mesoporous Organosilicas

J. Phys. Chem. B, Vol. 109, No. 21, 2005 **10733**

Figure 10. TEM micrographs of (a) MSE41 taken with direction of observation perpendicular to the pore axis; (b) MSE41 taken with direction of observation parallel to the pore axis, the dashed hexagon highlights the shape of their basal planes; (c) MSE40 taken with direction of observation perpendicular to the pore axis; (d) MSE40 taken with direction of observation parallel to the pore axis, the dashed circle highlights the shape of their basal planes; (e) MSE4; and (f) MSE42. Ultrathin sections (~50 nm) of sample MSE40 and MSE42 embedded in an epoxy resin were prepared by ultramicrotomy before being deposited on a carbon-coated copper grid.

salts during synthesis.[37] Many other factors, such as the surfactant/silica ratio,[63] the hydrolysis, and the condensation rate of the silica precursor,[37] are also important elements in controlling the curvature of the shape of mesoporous silicas. In this study, the trend of increasing curvature with increasing pH is believed to be similar to those reported by Ozin et al.[44−46] Unlike OS4 and OS6, the highly curved rods of OS2 are dispersed and often broken, which is believed to be due to the shearing of the stirring.

4.3. Formation of Cobweblike Network. Shown in Figure 9a are two short cylindrical particles of sample MSE5 and the surrounding nanofibers. A higher magnification image of the cobweblike networks (Figure 9b) shows that the nanofibers are actually made up of one or several mesopore channels with inner diameters comparable with those of the hexagonal pore channels. Thus, by a similar reasoning proposed above, it is believed that these nanofibers were grown from the many organosilicate-micelles or organosilicate liquid-crystal embryos that were not nucleated or accreted into large organosilicate crystals because of passivation, which is more rapid at high-acid concentrations. Therefore, it is reasonable to assume that more passivated organosilicate-micelles or embryos were formed at high-acid concentrations and the cobweb and surface corrugation on

material MSE4 and MSE5 was due to the random and loose deposition of these organosilicate-micelles or embryos on the ropelike macrostructures.

However, unlike those observed under FE-SEM, the nanofibers seen under TEM are less resolved, probably because of the overlapping of the projections of many fibers under the electron beam. The small spaces resulting from the intervening of the nanofibers and their effect on the secondary porosity of the materials were discussed previously.[64]

4.4. Formation of Rod-, Diamond-, and Platelike Particles. The TEM images of samples MSE40, MSE4, MSE41, and MSE42 shown in Figure 10 are in agreement with the observations under FE-SEM (see Figure 5). An illustration of the morphological transformation with respect to Si/P123 molar ratio is given in Figure 11. For MSE40, the growth of the organosilicate liquid crystal along the longitudinal axis or [001] was preferred over the growth along the transverse axes; this favored the development of a rodlike particle with relative high aspect ratio. The cross section of the rodlike particles of MSE40 is circular, which shows that the growth along the transverse axes is fast and isotropic. The diffuse regions seen around the rodlike particles are nanofibers and surface corrugations, which were
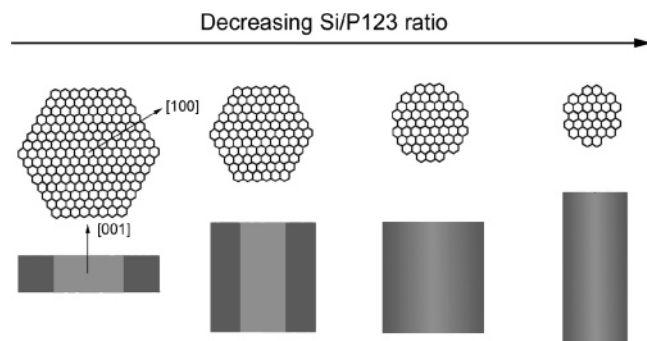
Figure 11. Schematic illustration of the dimension-controlled growth of the SBA-15 PMOs from rodlike to platelike morphology.

believed to be developed in a same manner as those of material MSE4.

As the Si/P123 ratio was increased, the growth along ⟨100⟩ became preferential and gradually dominated over the growth along other transverse axes and the longitudinal axis. This is reflected in the shape transformation of their particles from rods (MSE40) to particulates (MSE4, MSE41) and finally to platelets (MSE42) and a circular to hexagonal transition for the cross sections of the particles (Figure 11). Such a shape transformation is accompanied by the gradual elimination of surface corrugation and nanofibers.

It is known that the effectiveness of the nucleation and accretion processes are subject to the efficiency of the hydrolysis and polymerization of silicate species.[37] In this study, intermicellar organosilicate polymerization begins to play an important role when organosilicate-micelles are developed into a substantial amount, which not only nurtures the organosilicate liquid-crystal embryos or nuclei but also facilitates the accretion of the embryos into crystals. In an acid-mediated environment, the monomer organosilica precursors hydrolyze to form monomeric organosilicates, which further polymerize to give oligomeric organosilicates in the solution. Meanwhile, such oligomerization is also going on between the organosilicate species of the silicate-micelle rods, but in a more vigorous manner because of the local enrichment effects.[59,65] In other words, the free monomeric or oligomeric organosilicate species in the solution are active for a longer time because of their relatively slower condensation rates. Thus, it is reasonable to assume that these free monomeric and oligomeric organosilicates can act as important binding materials, or *inorganic glues*, between the organosilicate-micelles for the formation of amorphous organosilica walls and thus kinetically and thermodynamically influence the intermicellar organosilicate polymerization.[66]

In our experiments, the increased Si/P123 ratio, and consequently the increased free organosilicates or inorganic glues in the solution, had three major impacts on the organosilica crystal growth. First, it promoted the growth along the transverse axes. In addition, the growth of the nuclei along ⟨100⟩ was preferable over the other transverse axes, leading to a more thermodynamically favored hexagonal cross section. Second, the passivation of the organosilicate-micelles was able to anchor on the crystals along the ⟨100⟩ direction in the presence of these inorganic glues, thus eliminating the nanofiber and surface corrugations. Third, an excess amount of free inorganic glues could cause melting between the particles, as what happened to sample MSE42.

4.5. Particle Self-Assembly. To elucidate the self-assembly of the organosilica particles into necklacelike wires and to find out the details of the nanofiber formation, samples precipitated at different times during the formation of material MSE3 were separated and subjected to FE-SEM analyses. Material MSE3
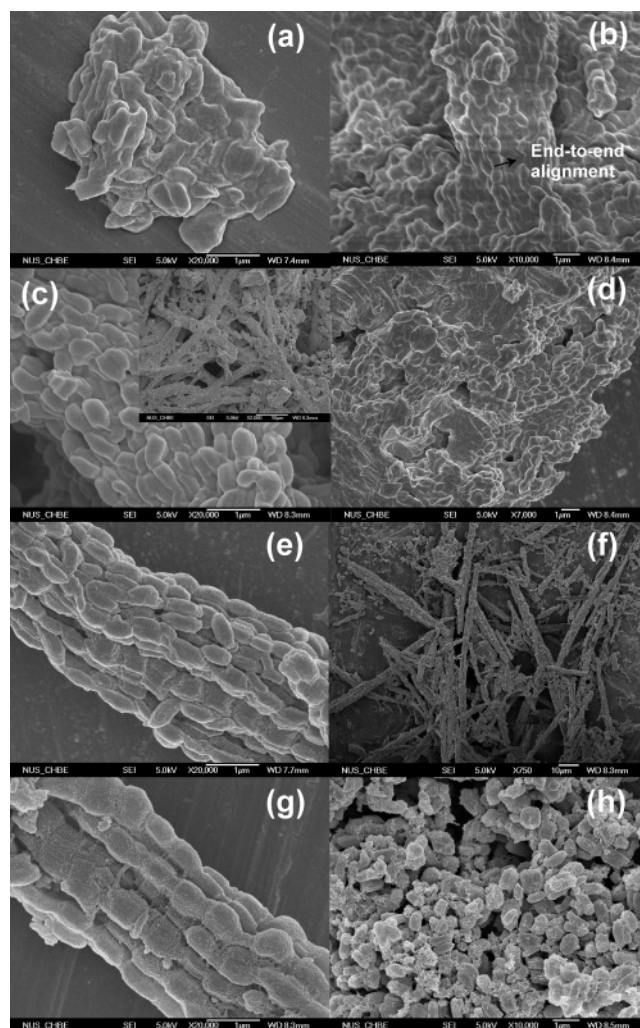

Figure 12. TEM micrographs of (a) MSE3-5h; (b) MSE3-7.6h; (c) a PMO rope of sample MSE3-9.6h, insert of c shows the aggregation of the PMO ropes; (d) ill-assembled spindlelike particles of MSE3-9.6h; (e) the ropes of sample MSE3-24h; (f) a rope of sample MSE3-24h; (g) MSE3; and (h) MSE3static.

was chosen because of the presence of both spindlelike particles and a small amount of nanofibers (see Figure 2c). Precipitate was observed after 4 h reaction, and the reaction mixture became highly turbid after 5 h. Figure 12 shows the FE-SEM images of samples MSE3 and MSE3-*t*h. The difference between MSE3 and MSE3-*t*h materials lies in that samples MSE3-*t*h were not autoclaved while MSE3 was prepared by autoclaving at 100 °C for 120 h.

The morphology of material MSE3-5h is cakelike with spindlelike particles randomly aggregated into a large particle with little sign of any alignment of the spindlelike particles (Figure 12a). It is believed that these particles are isolated in the synthetic liquid phase and that the cakelike macrostructure was formed during filtration. When concentrated during filtration, the particles melted together because of the silanol groups on the external surfaces of the particles and the softness of the particles at such an early stage of the reaction. Similar macrostructure to that of MSE3-5h is seen on sample MSE3-7.6h except for some end-to-end alignments between the spindlelike particles. Ropelike morphology constituting end-to-end assembly of spindlelike particles became predominant for sample MSE3-9.6h (Figure 12c). Nevertheless, a small proportion of ill-assembled spindlelike particles, akin to those observed on samples MSE3-5h and MSE3-7.6h, is still seen (Figure 12d).

Morphologies of Periodic Mesoporous Organosilicas

J. Phys. Chem. B, Vol. 109, No. 21, 2005 **10735**

The ropes, after filtration, aggregated together to form large chunks (Figure 12c, insert). This is due to the presence of surface silanol groups on the particles, which, during filtration, glued the ropes together.

For material MSE3-24h, separated ropes are clearly seen (Figure 12e), indicating a decreased amount of silanols groups on the surface of the particles before filtration. This is reasonable as the degree of condensation increased with reaction time. Compared with those obtained earlier, the spindlelike particles on the ropes of MSE3-24h are characterized by an improved regularity of the end-to-end alignment (Figure 12f). In addition, the sizes of each individual spindlelike particle of MSE3-24h are comparable with those of MSE3-5h, indicating that the growth of the crystal had almost ceased at the early stage of the reaction.

Despite the end-to-end alignment, little end-to-end fusion of the spindlelike particles is seen on material MSE3-24h. Material MSE3 (Figure 12g), obtained after an autoclaving period of 120 h, is marked by its end-to-end fusion of the spindlelike particles and a resumed growth in the size of the spindlelike particles, demonstrating the importance of hydrothermal treatment on the interconnection of the spindlelike particles. Noticeably, a trivial amount of nanofibers and slight surface corrugation were seen on sample MSE3, while they were not found on material MSE3-24h. Therefore, it is clear that the nanofibers and surface corrugation were also formed during the autoclaving period. The high autoclaving temperature of 100 °C compared with the aging temperature of ∼40 °C promoted further condensation of the organosilicate species, thus leading to enhanced interconnection of the spindlelike particles and deposition of the passivated organosilicate-micelles onto the spindlelike particles. Those organosilicate-micelles deposited on the surface of the spindlelike particles contributed to the growth of the particles, but in a less ordered manner, resulting in the formation of surface corrugations. The organosilicate-micelles deposited on the particle interstitial spacers resulted in the formation of nanofibers.

The particle morphology of MSE3static is displayed in Figure 12h. Randomly oriented spindlelike particles without any alignment can be seen, confirming that the end-to-end alignment is due to the shearing flow induced by stirring.[55] In addition, the spindlelike particles of MSE3static are less uniform in morphology and size than sample MSE3, which is probably due to the poor diffusion of the primary particles without stirring.

5. Conclusions

The effects of synthetic conditions such as stirring, acidity, reaction ratio, reaction duration, and autoclaving on the external morphologies of SBA-15 PMOs have been carefully studied in comparison with the SBA-15 PMSs. A wide spectrum of novel shapes, such as the spindle-, pearl-, diamond-, rod-, and platelike particles, and nanoparticles had been prepared with high yield. In particular, dimension control of these particles could be easily achieved by tuning their synthetic parameters. A nucleation-accretion mechanism based on rodlike organosilicate-micelle building blocks was proposed to explain the formation of these shapes by examining the relation between the external morphologies and the underlying mesostructure by transmission electron microscopy. In addition, the solution-phase self-assembly of these particles leads to a variety of large hierarchical macrostructures, such as mesostructured necklaces, cobweb-entrapped necklaces, and so forth. Stirring, reaction duration, and autoclaving were identified to be the key factors affecting the efficiency and degree of such self-assembly. Such under-

standings are useful for constructing mesoporous organosilicas with various well-defined, dimensionally controlled building blocks and their hierarchically assembled macrostructures.

References and Notes

(1) Kresge, C. T.; Leonowicz, M. E.; Roth, W. J.; Vartuli, J. C.; Beck, J. S. *Nature* **1992**, *359*, 710.
(2) Inagaki, S.; Guan, S.; Fukushima, Y.; Ohsuna, T.; Terasaki, O. *J. Am. Chem. Soc.* **1999**, *121*, 9611.
(3) Melde, B. J.; Holland, B. T.; Blanford, C. F.; Stein, A. *Chem. Mater.* **1999**, *11*, 3302.
(4) Asefa, T.; MacLachlan, M. J.; Coombs, N.; Ozin, G. A. *Nature* **1999**, *402*, 867.
(5) Burleigh, M. C.; Markowitz, M. A.; Wong, E. M.; Lin, J. S.; Gaber, G. P. *Chem. Mater.* **2001**, *13*, 4411.
(6) Muth, O.; Schellbach, C.; Froba, M. *Chem. Commun.* **2001**, 2032.
(7) Cho, E. B.; Kwon, K. W.; Char, K. *Chem. Mater.* **2001**, *13*, 3837.
(8) Kaliaguine, S.; Hamoudi, S. *Chem. Commun.* **2002**, 2118.
(9) Matos, J. R.; Kruk, M.; Mercuri, L. P.; Jaroniec, M.; Asefa, T.; Coombs, N.; Ozin, G. A.; Kamiyama, T.; Terasaki, O. *Chem. Mater.* **2002**, *14*, 1903.
(10) Guo, W. P.; Kim, I.; Ha, C. S. *Chem. Commun.* **2003**, 2692.
(11) MacLachlan, M. J.; Asefa, T.; Ozin, G. A. *Chem.—Eur. J.* **2000**, *6*, 2507.
(12) Asefa, T.; Yoshina-Ishii, C.; MacLachlan, M. J.; Ozin, G. A. *J. Mater. Chem.* **2000**, *10*, 1751.
(13) Kickelbick, G. *Angew. Chem., Int. Ed.* **2004**, *43*, 3102.
(14) Inagaki, S.; Guan, S.; Ohsuna, T.; Terasaki, O. *Nature* **2002**, *416*, 304.
(15) Landskron, K.; Hatton, B. D.; Perovic, D. D.; Ozin, G. A. *Science* **2003**, *302*, 266.
(16) Burleigh, M. C.; Markowitz, M. A.; Jayasundera, S.; Spector, M. S.; Thomas, C. W.; Gaber, B. P. *J. Phys. Chem. B* **2003**, *107*, 12628.
(17) Lu, Y.; Fan, H.; Doke, N.; Loy, D. A.; Assink, R. A.; LaVan, D. A.; Brinker, C. J. *J. Am. Chem. Soc.* **2000**, *122*, 5258.
(18) Bhaumik, A.; Kapoor, M. P.; Inagaki, S. *Chem. Commun.* **2003**, 470.
(19) Kapoor, M. P.; Sinha, A. K.; Seelan, S.; Inagaki, S.; Tsubota, S.; Yoshida, H.; Haruta, M. *Chem. Commun.* **2002**, 2902.
(20) Doménech, A.; Alvaro, M.; Ferrer, B.; García, H. *J. Phys. Chem. B* **2003**, *107*, 12781.
(21) Sakamoto, Y.; Fukuoka, A.; Higuchi, T.; Shimomura, N.; Inagaki, S.; Ichikawa, M. *J. Phys. Chem. B* **2004**, *108*, 853.
(22) Baleizão, C.; Gigante, B.; Das, D.; Alvaro, M.; Garcia, H.; Corma, A. *Chem. Commun.* **2003**, 1860.
(23) Burleigh, M. C.; Jayasundera, S.; Spector, M. S.; Thomas, C. W.; Markowitz, M. A.; Gaber, B. P. *Chem. Mater.* **2004**, *16*, 3.
(24) Zhao, D.; Huo, Q.; Feng, J.; Chmelka, B. F.; Stucky, G. D. *J. Am. Chem. Soc.* **1998**, *120*, 6024.
(25) Zhu, H. G.; Jones, D. J.; Zajac, J.; Roziere, J.; Dutartre, R. *Chem. Commun.* **2001**, 2568.
(26) Guo, W. P.; Park, J. Y.; Oh, M. O.; Jeong, H. W.; Cho, W. J.; Kim, I.; Ha, C. S. *Chem. Mater.* **2003**, *15*, 2295.
(27) Wang, W.; Xie, S.; Zhou, W. Sayari, A. *Chem. Mater.* **2004**, *16*, 1756.
(28) Bao, X. Y.; Zhao, X. S.; Li, X.; Chia, P. A.; Li, J. *J. Phys. Chem. B* **2004**, *108*, 4684.
(29) Fan, J.; Lei, J.; Wang, L. M.; Yu, C. Z.; Tu, B.; Zhao, D. Y. *Chem. Commun.* **2003**, 2140.
(30) Lei, J.; Fan, J.; Yu, C. Z.; Zhang, L. Y.; Jiang, S. Y.; Tu, B.; Zhao, D. Y. *Microporous Mesoporous Mater.* **2004**, *73*, 121.
(31) Shio, S.; Kimura, A.; Yamaguchi, M.; Yoshida, K.; Kuroda, K. *Chem. Commun.* **1998**, 2461.
(32) Gallis, K. W.; Araujo, J. T.; Duff, K. J.; Moore, J. G.; Landry, C. C. *Adv. Mater.* **1999**, *11*, 1452.
(33) Loerke, J.; Marlow, F. *Adv. Mater.* **2002**, *14*, 1745.
(34) Boissiere, C.; Larbot, A.; van der Lee, A.; Kooyman, P. J.; Prouzet, E. *Chem. Mater.* **2000**, *12*, 2902.
(35) Schmidt-Winkel, P.; Yang, P. D.; Margolese, D. I.; Chmelka, B. F.; Stucky, G. D. *Adv. Mater.* **1999**, *11*, 303.
(36) Yu, C. Z.; Fan, J.; Tian, B. Z.; Zhao, D. Y.; Stucky, G. D. *Adv. Mater.* **2002**, *14*, 1742.
(37) Zhao, D. Y.; Sun, J. Y.; Li, Q. Z.; Stucky, G. D. *Chem. Mater.* **2000**, *12*, 275.
(38) Yang, P. D.; Zhao, D. Y.; Chmelka, B. F.; Stucky, G. D. *Chem. Mater.* **1998**, *10*, 2033.
(39) Marlow, F.; Kleitz, F. *Microporous Mesoporous Mater.* **2001**, *44*, 671.

(40) Grün, M.; Lauer, I.; Unger, K. K. *Adv. Mater.* **1997**, *9*, 254.

(41) Yang, H.; Vovk, G.; Coombs, N.; Sokolov, I.; Ozin, G. A. *J. Mater. Chem.* **1998**, *8*, 743.

(42) Lu, Y. F.; Fan, H. Y.; Stump, A.; Ward, T. L.; Rieker, T.; Brinker, C. J. *Nature* **1999**, *398*, 223.

(43) Martin, T.; Galarneau, A.; Di Renzo, F.; Fajula, F.; Plee, D *Angew. Chem., Int. Ed.* **2002**, *41*, 2590.

(44) Yang, H.; Coombs, N.; Ozin, G. A. *Nature* **1997**, *386*, 692.

(45) Yang, H.; Ozin, G. A.; Kresge, C. T. *Adv. Mater.* **1998**, *10*, 883.

(46) Yang, S. M.; Yang, H.; Coombs, N.; Sokolov, I.; Kresge, C. T.; Ozin, G. A. *Adv. Mater.* **1999**, *11*, 52.

(47) Lin, H. P.; Mou, C. Y. *Science* **1996**, *273*, 765.

(48) Rana, R. K.; Mastai, Y.; Gedanken, A. *Adv. Mater.* **2002**, *14*, 1414.

(49) Chao, M. C.; Wang, D. S.; Lin, H. P.; Mou, C. Y. *J. Mater. Chem.* **2003**, *18*, 2853.

(50) Guan, S.; Inagaki, S.; Ohsuna, T.; Terasaki, O. *J. Am. Chem. Soc.* **2000**, *122*, 5660.

(51) Sayari, A.; Hamoudi, S.; Yang, Y.; Moudrakovski, I. L.; Ripmeester, J. R. *Chem. Mater.* **2000**, *12*, 3857.

(52) Park, S. S.; Lee, C. H.; Cheon, J. H.; Park, D. H. *J. Mater. Chem.* **2001**, *11*, 3397.

(53) Rebbin, V.; Jakubowski, M.; Pötz, S.; Fröba, M. *Microporous Mesoporous Mater.* **2004**, *72*, 99.

(54) Yu, C. Z.; Fan, J.; Tian, B. Z.; Zhao, D. Y. *Chem. Mater.* **2004**, *16*, 889.

(55) Kosuge, K.; Sato, T.; Kikukawa, N.; Takemori, M. *Chem. Mater.* **2004**, *16*, 899.

(56) Azároff, L. V. *Introduction to Solids*; McGraw-Hill: New York, 1960.

(57) Sadasivan, S.; Khushalani, D.; Mann, S. *J. Mater. Chem.* **2003**, *13*, 1023.

(58) Sadasivan, S.; Fowler, C. E.; Khushalani, D.; Mann, S. *Angew. Chem., Int. Ed.* **2002**, *41*, 2151.

(59) Firouzi, A.; Kumar, D.; Bull, L. M.; Besier, T.; Sieger, P.; Huo, Q.; Walker, S. A.; Zasadzinski, J. A.; Glinka, C.; Nicol, J.; Margolese, D.; Stucky, G. D.; Chmelka, B. F. *Science* **1995**, *267*, 1138.

(60) Regev. O *Langmuir* **1996**, *12*, 4940.

(61) Lee, Y. S.; Surjadi, D.; Rathman, J. F. *Langmuir* **1996**, *12*, 6202.

(62) Marlow, F.; Spliethoff, B.; Tesche, B.; Zhao, D. *Adv. Mater.* **2000**, *12*, 961.

(63) Leonard, A.; Blin, J. L.; Robert, M.; Jacobs, P. A.; Cheetham, A. K.; Su, B. L. *Langmuir* **2003**, *19*, 5484.

(64) Bao, X. Y.; Zhao, X. S.; Qiao S. Z.; Bhatia, S. K. *J. Phys. Chem. B* **2004**, *108*, 16441.

(65) Monnier, A.; Schuth, F.; Huo, Q.; Kumar, D.; Margolese, D.; Maxwell, R. S.; Stucky, G. D.; Krishnamurty, M.; Petroff, P.; Firouzi, A.; Janicke, M.; Chmelka, B. F. *Science* **1993**, *261*, 1299.

(66) Zhou, W. Z.; Klinowski, J. *Chem. Phys. Lett.* **1998**, *292*, 207.